Atmos. Chem. Phys. Discuss., 10, 25389–25433, 2010
www.atmos-chem-phys-discuss.net/10/25389/2010/
doi:10.5194/acpd-10-25389-2010

Atmospheric Chemistry and Physics Discussions

Satellite observations of aerosol transport from East Asia to the Arctic: three case studies

M. Di Pierro, L. Jaeglé, and T. L. Anderson

Department of Atmospheric Sciences, University of Washington, Seattle, Washington, USA

Received: 24 September 2010 – Accepted: 19 October 2010 – Published: 1 November 2010

Correspondence to: M. Di Pierro (dipierro@atmos.washington.edu)

Published by Copernicus Publications on behalf of the European Geosciences Union.

Abstract

Vertical profiles of aerosols obtained with the CALIOP lidar onboard CALIPSO are used in conjunction with the GEOS-Chem chemical transport model and NOAA's HYSPLIT trajectory model to document three aerosol export events from East Asia to the Arctic that occurred in the year 2007. During each of these events CALIOP sampled the pollution plumes multiple times over periods of five to seven days. Meridional transport to the Arctic was rapid, taking 3–4 days and was accompanied by net diabatic heating of ~5 °C/day and precipitation in its ascending stage. Once in the Arctic transport was nearly isentropic with slow subsidence and radiative cooling at a rate of 1–1.5 °C/day. We find close agreement between modeled and observed plume in terms of length, altitude, thickness and, within the measurement uncertainties, extinction coefficient. In one event the satellite algorithm misclassifies the aerosol layer as ice clouds as a result of the relatively high depolarization ratio (0.06), likely caused by a somewhat high dust component in the aerosol mixture. The misclassification is more severe at daytime (67% of layers are misclassified) than at nighttime (32%). The two most intense export events occurred in early spring within a three-week time span and are strongly related to a persisting blocking anticyclone that was located in the NW Pacific. Using 500 hPa geopotential height anomalies of these two events along with several others in 2007–2009 we develop a meteorological index that captures 40–60% of the variance of Asian transport events to the Arctic in winter and spring.

1 Introduction

Starting in the 1950s, weather reconnaissance flights over the Arctic revealed the existence of a haze that could extend over vast areas (Mitchell, 1956). This phenomenon became later known as Arctic Haze. Chemical analyses of the aerosol matter showed that the haze was predominantly composed of sulfate and particulate organic matter in addition to smaller quantities of black carbon, ammonium, nitrate, and dust aerosols,

ACPD
10, 25389–25433, 2010

and several anthropogenic pollutants such as heavy metals and condensed volatile organic carbon compounds (Quinn et al., 2002).

Arctic Haze has long been attributed to transport of pollution from mid-latitude sources (Shaw, 1995). Chemical transport models (CTMs) show the dominant role of Europe and Russia as sources of low-level aerosol pollutants to the Arctic, but also show that East Asian and North American aerosols make a significant fractional contribution in the middle to upper troposphere during winter and spring (Klonecki et al., 2003; Koch and Hansen, 2005).

Transport to the Arctic is largely mediated by the Polar Dome, a tropospheric barrier of isentropic surfaces closing around the Arctic. If the transport is adiabatic, air parcels follow the northward sloping surfaces and necessarily have to ascend (Carlson, 1981). Also, following this argument, a warm air mass will ascend more than a cooler one when traveling from the mid-latitudes to the Arctic. Springtime transport of North American and East Asian sources to the Arctic generally occurs by export from the boundary layer in the warm conveyor belt of mid-latitude cyclones, followed by poleward transport along sloping isentropes in the free troposphere, and entrance into the polar dome from above by means of radiative cooling (Klonecki et al., 2003; Stohl, 2006). In contrast, northern Eurasian emissions tend to be transported at lower levels to the Arctic. Indeed, rapid low-level transport can be associated with a significant poleward retreat of the polar front in the presence of a blocking event or by prolonged flow over cold, snow-covered land masses causing strong diabatic cooling (Iversen and Joranger, 1985; Klonecki, 2003; Stohl, 2006).

In a recent CTM inter-comparison study, Shindell et al. (2008) demonstrated that the relative importance of different regions as aerosol sources for the Arctic is consistent across models, but that the absolute concentrations vary significantly. These discrepancies are linked to uncertainties in model representations of aerosol physical and chemical processes, but also to model-to-model variations in transport in the middle and upper troposphere. The scarceness of Arctic observations in the free troposphere has hindered the evaluations of models in that region. While there have been a

ACPD
10, 25389–25433, 2010

number of recent aircraft campaigns targeting the Arctic (TOPSE, ARCTAS, ARCPAC and POLARCAT), most took place in the North American or European sector of the Arctic. Thus the Siberian sector, where models predict a dominant influence of Asian aerosols, remains unrepresented.

In this study, we use Arctic observations of the vertical distribution of aerosols from the Cloud-Aerosol Lidar with Orthogonal Polarization (CALIOP) on board the CALIPSO satellite to examine three episodes of pollution export from East Asia to the Arctic, two during early spring and one in autumn. CALIOP has many advantages in the study of long-range transport of aerosols to the Arctic. Unlike passive satellite sensors (such as MODIS, MISR, PARASOL) it determines the precise vertical location of identified features and it can retrieve aerosol properties during the night as well as the day and over highly reflective ice and snow surfaces. Its main limitations are that it only samples directly beneath the satellite (i.e. zero swath width) and that it can not detect aerosols located beneath optically thick clouds. We combine CALIOP retrievals of aerosol attenuated backscatter and extinction, together with the GEOS-Chem model and back-trajectory calculations to track the transport pathway and evolution of these three Asian plumes. Section 2 presents a description of GEOS-Chem, CALIOP and the lagrangian trajectory model. The three case studies are presented in Sect. 3. A discussion follows in Sect. 4, where the case studies are placed in a broader context. Section 5 summarizes the results.

2 Numerical models and observations

2.1 GEOS-Chem chemical transport model

The GEOS-Chem global tropospheric chemistry model is driven by assimilated meteorological observations from the Goddard Earth Observing System (GEOS-5) of the NASA Global Modeling and Assimilation Office. We use version v8-02-04 of GEOS-Chem (http://acmg.seas.harvard.edu/geos/). The GEOS-5 meteorological fields are provided at 3 to 6 h temporal resolution. The native resolution of the meteorological

ACPD
10, 25389–25433, 2010

fields is 0.5×0.667° in the horizontal with 72 hybrid eta vertical levels, extending from the surface up to 0.01 hPa (~80 km), including 14 levels between the surface and 2 km altitude. For our simulations, we degrade the fields to a 2°×2.5° horizontal resolution and 47 vertical levels.

We conducted a fully coupled aerosol-oxidant simulation (Bey et al., 2001; Martin et al., 2003; Park et al., 2004) for 2007–2009. This simulation was initialized with a 1-year spin-up run. The aerosol simulation in GEOS-Chem represents the sulfate-nitrate-ammonium system (Park et al., 2004), organic and black carbon (Park et al., 2003; Liao et al., 2007), sea salt (Alexander et al., 2005), and mineral dust (Fairlie et al., 2007), as an external mixture. The aerosol extinction is calculated at 550 nm from Mie theory (Martin et al., 2003). This wavelength is close enough to CALIOP 532 nm channel to permit direct comparison between the two variables.

Global anthropogenic emissions are from the EDGAR 3.2FT2000 database (Olivier and Berdowski, 2001) for 2000. Over Asia, these emissions are overwritten with the emission inventory of Zhang et al. (2009) corresponding to the year 2006, with annual anthropogenic and biofuel emissions of 47.1 Tg SO_2 , 2.97 Tg black carbon, and 6.57 Tg organic carbon. Dust emissions are based on a dust mobilization scheme that takes into account seasonal devegetation (Zender et al., 2003). Biomass burning emissions are taken from the GFEDv2 monthly inventory (Van der Werf et al., 2006).

In addition to the standard aerosol-oxidant simulation, we conducted a sensitivity simulation in which we turned off anthropogenic sources of aerosols and their precursors over Asia (defined here as 70–180° E; 8–70° N). We also turned off Asian dust sources in the region 42–152.5° E, 20–88° N. The simulation was first spun up for 1 year starting in 2006, and the results were archived for 2007–2009. We infer the Asian contribution to the aerosol optical depth (AOD) by subtraction between the standard simulation and the sensitivity simulation with Asian anthropogenic aerosol sources and dust sources turned off. The resulting AOD will be referred to as "Asian AOD". In the discussion we will also refer to the anthropogenic sulfate component of the Asian AOD as "Asian Sulfate AOD", and to the Asian AOD dust component as "Asian Dust AOD".

ACPD
10, 25389–25433, 2010

For comparison to CALIOP observations, we sample the model along the CALIPSO orbit tracks, extracting 1-h time resolution tracer fields obtained from the original fields by linear interpolation. Thus, the observed and model scenes always coincide to within thirty minutes.

2.2 CALIOP lidar measurements

The CALIPSO satellite was launched on 28 April 2006 and is part of the sun-synchronous A-train constellation of satellites, which orbit at 705 km above mean sea level (a.m.s.l.) at an inclination of 98°, and complete 14.55 orbits a day crossing the equator at 01:30 p.m. local time. The CALIOP lidar is the main instrument on board CALIPSO. The lidar pulse is simultaneously emitted at 532 nm and 1064 nm providing vertically resolved attenuated backscatter profiles of the atmosphere at both wavelengths. A polarization beam splitter allows measurements of the parallel and perpendicular components of the 532 nm return (Winker et al., 2004). The two channels and polarization information aid in discriminating between clouds and aerosols. CALIOP's strength lies in its high vertical resolution, 30 (60) m in the lower troposphere at 532 (1064) nm, decreasing with height but still no less than 60 m for both channel below 20.2 km altitude. The maximum horizontal resolution is 333 m, corresponding to one lidar shot. However, a single atmospheric return is noisy, so several consecutive profiles are averaged to increase the signal-to-noise ratio and allow retrieval of faint features, such as aerosol layers far from their source region (Vaughan et al., 2004). Nighttime retrievals are characterized by a higher lidar signal-to-noise ratio than during daytime, thus higher accuracy is achieved at night in terms of locating the boundaries of the layers and retrieving optical properties.

The measured Level-1 attenuated return signal is analyzed by three consecutive algorithms, which locate the feature, classify it into cloud or aerosol and solve for its optical properties (Winker et al., 2009). A multi-scale approach is employed to locate the features at increasing horizontal averaging of 1, 5, 20 and 80 km (Vaughan et al., 2004; Winker et al., 2009) and the results are archived in Level-2 products.

ACPD
10, 25389–25433, 2010

The third of these algorithms solves the inversion problem that consists in deriving optical properties from the measured signal. The measured attenuated backscatter depends on the inherent backscatter of the feature being measured but also on the attenuation by molecules and particles overlying it. Since the inversion problem is underdetermined, additional uncertainties are introduced by this technique itself, largely ascribed to the assumed value of extinction to backscatter ratio, or lidar ratio, used to initiate the retrievals (Young et al., 2008). The associated uncertainty in extinction coefficient is reported to be ±40% based on a 30% lidar ratio uncertainty (see http://www-calipso.larc.nasa.gov/products/). The retrieved optical properties are available in two formats: Level-2 Layer products and Profile products. The Level-2 Layer products contain information on the spatial distribution (i.e. top and bottom of individual features) and integrated optical properties of all aerosol and cloud features detected. In the Level-2 Profile products each atmospheric column is vertically resolved for its optical properties at a vertical resolution between −0.5 and 20.2 km of 60–120 m, depending on the data version.

The performance of the aerosol-cloud discrimination algorithm has been assessed on a global basis based on expert manual classification performed over one day of data (Liu et al., 2009). A fraction of 3–4% percent of aerosol layers are erroneously classified as clouds, which is roughly comparable to the fraction of cloud layers erroneously classified as aerosols. Under daytime conditions, misclassification of aerosols as clouds is more frequent than at nighttime, whereas the opposite occurs for the misclassification of clouds as aerosols. These issues will be addressed in more detail over the Arctic in this paper (Sect. 3.2.3).

In our study, we used version 2.01 Level-2 Cloud (5-km) and Aerosol (40-km) Profile products to perform comparisons between CALIOP and GEOS-Chem aerosol extinction profiles. The plume optical properties are extracted from 5-km Aerosol Layer and Cloud Layer products. In one case where a misclassification of aerosol into cloud occurs, we also employ Level-1 (version 3.01) profiles of attenuated backscatter under clear-sky conditions above the plume to perform a comparison with the model.

ACPD
10, 25389–25433, 2010

2.3 HYSPLIT Lagrangian Trajectory model

We used the NOAA Air Resources Laboratory Lagrangian Trajectory model HYSPLIT version 4.9 (Draxler, 2004) to calculate back trajectories and identify the source of the aerosols observed over the Arctic. In our simulations, HYSPLIT is driven by the NCEP (National Centers for Environmental Prediction) GDAS (Global Data Assimilation System) fields which are produced at 3 hourly temporal resolution, 1°×1° horizontal resolution and 23 vertical levels from 1000 to 20 hPa. When used to calculate parcel trajectories HYSPLIT includes 3-D turbulent components to simulate dispersion (Draxler, 2004). We employed model vertical velocity fields rather than constraining the transport to occur on isentropic surfaces. Each cross-section of an aerosol plume that is observed by the CALIOP lidar is sampled by taking the mid-point of each 5-km horizontal layer belonging to the plume. A random subset of 50 points is then extracted from the observed plume and back trajectories are run for 10 days.

3 Case studies

We visually inspected CALIOP Level-2 observations for the year 2007 over the Arctic using the GEOS-Chem model simulation to locate large Asian aerosol transport events. We then selected three events during which the aerosol plumes were intercepted multiple times by the CALIPSO orbit tracks: 28 February–4 March; 12–19 March and 20–27 October, 2007.

3.1 28 February–4 March 2007 pollution export episode

This event was the most intense of the three presented here. Due to the large horizontal extent of the aerosol haze layer (spanning more than 100° longitude), the CALIPSO orbits intercepted it 23 times over this 5-day period.

ACPD
10, 25389–25433, 2010

3.1.1 Morphology and optical properties of the pbserved haze layers

Figure 1 shows the locations of the haze layers observed by CALIOP during the 28 February–4 March period. The CALIPSO orbits are drawn with a dashed line and their segments in the haze layer are in red. The layers were first observed over the East Siberian Arctic sector on 28 February, and then slowly drifted east to the North American sector. Table 1 presents a summary of the latitude/longitude range, height, aerosol optical depth (AOD), integrated volume depolarization ratio (IVDR) and integrated attenuated color ratio (ratio between attenuated backscatter at 1064 nm and 532 nm, henceforth simply referred to as color ratio) for the 23 plume cross sections observed by CALIOP during this event. Figure 2 displays a subset of five CALIOP and GEOS-Chem aerosol extinction cross sections of the haze event. The CALIOP features classified as aerosols are displayed with the purple-green-red color bar while the clouds are indicated in the grayscale color bar. The aerosol layers appear as thin elongated features ranging in thickness from 500 to 2000 m and individual segments had a length of 160 km to 1845 km (Table 1). The altitude of the features ranged from 1.5–4.5 km altitude at lower latitudes (60–70° N) increasing to 2.0–6.5 km poleward of 70° N.

The ascending shape of the aerosol plumes shown on Fig. 2a is characteristic of transport along sloping isentropes. The northward tilt of the aerosol layers is consistent with the local configuration of potential temperature surfaces (dashed lines on Fig. 2a). The tilt is higher than the potential temperature surface slope in some instances, e.g. panel c in Fig. 2a, indicating that various parts of the plume were emitted from sources at different potential temperatures and also underwent different histories of diabatic processes. In the case of panel b (Fig. 2a), the lack of tilt is associated with a local flattening of the isentropes.

By integrating the CALIOP extinction over the length and height of individual plumes, we find AOD ranging from 0.01 to 0.08, with a mean of 0.038 for all observations (Table 1). If we integrate over the entire vertical column (0–10 km) the mean AOD

ACPD
10, 25389–25433, 2010

increases to 0.046. The plume displays fairly uniform values of IVDR, with most values below 0.03, indicating small particles and relatively small amounts of dust. Indeed, because of their large size and non-sphericity, dust aerosols exhibit the highest depolarization ratio (IVDR>0.06) of all aerosol species, while other aerosols have a much lower depolarization ratio (Liu et al., 2008). Values of the color ratio (0.21–0.36) are also small, indicating sub-micron size, typical of pollution aerosols or smoke.

3.1.2 Asian origin and meteorology of the event

The backtrajectories corresponding to each observed aerosol layer are shown on Fig. 1. We are only displaying trajectories that originate in the boundary layer (defined here as reaching an altitude below 1500 m), which account for roughly half of the backtrajectories. Figure 1 shows that the plume originated from the boundary layer over NE China 4–8 days prior to observations. A small number of the displayed trajectories (6%) also appear to have been transported from the Gobi desert. The Asian origin of the haze event is confirmed by the GEOS-Chem Asian AOD simulation, with observed plumes located over areas with enhancements in Asian AOD (Fig. 1).

The observed airmasses ascended to 4–7 km altitude in 24 h and most of the ascent took place between 25 February 12Z and 27 February 0Z (Fig. 1, right panels). Potential temperature and precipitation computed along the trajectories shows that the initial stage of diabatic transport was associated with precipitation to the ground. This was followed by a dry nearly-isentropic transport, with gradual ascent following isentropic surfaces poleward of 67° N. We find that the departure from isentropy is due to radiative cooling at a rate of ∼1.5 °C/day, a value in agreement with previous studies (Curry, 1983; Carlson, 1981). The rapid variations in altitude seen in the backtrajectories between 55° N and 60° N (Fig. 1) are associated with orographic effects as parcels are traveling above the mountain ranges of southeastern Siberia at low altitudes.

Subsidence within the Arctic basin could be seen only for the last 16 h of the last plume on 4 March at 15:30 UTC, with a subsidence rate of ∼1 cm/s. No plume was observed to reach the surface. It is likely that the plumes dissipated to the point where their backscatter fell below CALIOP detection threshold even if subsidence continued.

ACPD
10, 25389–25433, 2010

This export event was triggered by a mid-latitude cyclone that formed on 21 February North of the Black Sea and began to travel eastward over continental Asia. On 23 February at 12:00 UTC, the cyclone reached its maximum intensity (987 hPa). It then began to weaken as it continued on its eastward route. A secondary cyclogenesis occurred as the low pressure center passed over the Altai mountain range, a region of active lee cyclogenesis (Chen et al., 1991). The pressure minimum decreased for two consecutive 6-h periods and reached a new minimum on 24 February at 12:00 UTC.

Figure 3 (left panels) shows the modeled Asian AOD, 500 hPa geopotential heights and 500 hPa winds for the 25–28 February time period. Sea level pressure and precipitation are displayed on the right panels. Geopotential heights and sea level pressure are from the NCEP-NCAR Reanalysis (Kalnay et al., 1996), whereas precipitation is from GEOS-5. The secondary cyclogenesis is reflected in the mid-tropospheric deepening of a secondary wave that becomes a full trough on 26 February, as shown in the two top panels of Fig. 3.

The low pressure center (marked with an L on the top right panel of Fig. 3) began to manifest its influence upon NE China on 25 February, when persistent warm advection anticipated the passage of a cold front. The station of Changchun (WMO Id: 54161; 43.9° N; 125.2° E) recorded the passage of a warm front between 24 February, 12:00 UTC and 25 February, 00:00 UTC, followed by a cold front (26 February, 00:00–12:00 UTC). In the early stages of the export the AOD enhancement is found on the east side of the surface low. Surface convergence around the low on 25 February provides the ascending motion by means of the warm conveyor belt of the sweeping cyclone which lifts the pollution to the middle troposphere. The aerosol-laden air mass underwent cloud processes and likely strong scavenging associated with the extensive cloud cover of the low pressure system. As a consequence of the cloud cover CALIPSO did not observe the aerosol plume until it emerged inside the Arctic. All precipitation during transport occurred south of 65° N.

ACPD
10, 25389–25433, 2010

The subsequent rapid poleward transport of the plume is associated with a split-flow blocking high pressure system (H on bottom left panels, Fig. 3) which began to form at the end of February in the NW Pacific and persisted until mid-March. This high led to a split-flow blocking with one branch moving north and one east over the Pacific and was responsible for the anomalous southerly flow during the period of the event.

3.1.3 Comparison between observed and modeled haze layers

The model generally reproduces both the horizontal and vertical location of the observed aerosol layer (Fig. 2a, Table 1). While the boundaries of the haze layer are well defined in the observations, they appear to be more spread-out in the model. This is likely to be due to the model finite horizontal and vertical resolution. Indeed, Rastigejev et al. (2010) demonstrated that CTMs tend to dilute pollution plumes as a result of numerical diffusion and stretching of the plume in complex geophysical flow. The apparent difference between model and observations could also be associated with the sensitivity of the CALIOP instrument. Winker et al. (2009) report a 532 nm backscatter sensitivity threshold for CALIOP nighttime retrievals at 80 km horizontal averaging of 2×10^{-4} km^{-1} sr^{-1} at 10 km altitude increasing to 4×10^{-4} km^{-1} sr^{-1} at the surface (see their Fig. 4). When we take into account this altitude-dependent sensitivity (by setting to zero model backscatter coefficients below the CALIOP detection threshold) the boundaries of the plume cross sections are more sharply defined (Fig. 2b). The thickness of the modeled aerosol layers remains somewhat wider than observed, likely due to the numerical diffusion and the fact that the layer thickness is similar to model vertical resolution (~200–500 m in the 2–6 km altitude range).

Figure 4 shows a comparison between satellite-retrieved and modeled mean extinction profiles averaged over the boxed regions of Fig. 2. We apply the CALIOP sensitivity threshold to the model extinction. In performing the horizontal averaging for both model and observations, we exclude atmospheric columns below the top of the CALIOP-detected clouds. The model generally captures the layer height and extinction observed by CALIOP. As summarized in Table 1, the model plume average AOD

ACPD
10, 25389–25433, 2010

(0.050) is higher than observations (0.038). When the altitude dependent sensitivity is applied in the model, we find a mean plume AOD of 0.038, in better agreement with observations. For the 0–10 km column, the observed and modeled AOD are 0.046 and 0.053, respectively.

The dominant aerosol species in the model is sulfate (>80% of the total extinction), while dust accounts for most of the remaining extinction (see Fig. 4). This is consistent with the low IDVR observed by CALIOP for this event. In the model, Asian aerosol sources contribute 40% of the total column AOD and 65% of the plume AOD.

3.2 12–19 March 2007 export episode

3.2.1 Morphology and optical properties of the observed haze layers

The first haze layer was observed by CALIOP on 12 March at 17:59 UTC. Thirty-six other layers were observed in the following days, until 19 March, as summarized in Table 2. Figure 5 illustrates the location of the haze layers that were observed by CALIOP for 14 through 18 March, as well as backtrajectories and altitude history of the parcels composing this haze event. The aerosol layers observed by CALIOP are at 3–4 km altitude. They initially start at 70–82° N above the East Siberian sector of the Arctic then slowly move towards the N. American sector. The layers have a mean thickness of ~3 km and length ranging from 320 to 1360 km (Table 2).

The depolarization ratio of these layers is often in excess of 0.06 (Table 2), indicating a strong dust component. We note that daytime (D) and nighttime (N) retrievals of IVDR and color ratio differ at 99% significance level, with nighttime values being systematically lower (IVDR:0.051 for N and 0.067 for D; color ratio: 0.25 for N and 0.32 for D, Table 2). Ice crystals may be responsible for the high depolarization ratio, but we rule out this possibility because the IVDR demonstrates remarkable constancy spatially and temporally, and the features persist for several days.

ACPD
10, 25389–25433, 2010

3.2.2 Meteorology

The event started with strongly descending northwesterly cyclonic flow from the plateaus of Mongolia to the Sea of Japan on 7–8 March 2007. This flow mobilized large amounts of dust which mixed in with pollution aerosols from NE China and accumulated over the Sea of Japan. The MODIS satellite onboard Terra (not shown) indicates elevated AOD over the Korean peninsula on 9 March and over the Sea of Japan on 10 March.

Figure 6 shows the evolution of the early stages of the export between 10 and 13 March. On 10 March, 12:00 UTC (Fig. 6, top panels), the GEOS-Chem model shows high Asian AOD values over the Sea of Japan. The formation of a cyclone over the NE coast of China on 10 March (labeled C in Fig. 6, right panels) led to the export of the pollution-dust mixture from the planetary boundary layer to the free troposphere. The 500 hPa geopotential heights show that a deep trough extended to NW China, with values falling below 5100 m. On 12 March at 12:00 UTC an elongated region of enhanced AOD separates from the cyclonic circulation and is quickly en route to the Arctic, by virtue of the strong zonal geopotential height gradient between the Siberian trough and the pronounced Omega blocking high (H in Fig. 6, left panels) in the North Pacific.

Roughly half of all backtrajectories corresponding to the haze layers observed by CALIOP originated in the boundary layer. Of these 90% came from East Asia and 10% came from the Gobi desert (Fig. 5). Ascent took place entirely outside the Arctic during the early stages of the cyclone development on 10 and 11 March; it was very intense with parcel rising to 4–8 km and precipitation reaching 4 mm/h (not shown). The transport was then characterized by slow but steady general subsidence (0.6 cm/s) that began as the plume reached the Arctic Ocean on 14 March and continued until the last cross section was observed on 19 March. Parcel potential temperature decreased at a fairly steady rate of 1.5–2 °C/day due to radiative cooling and possibly turbulent mixing with the surrounding air.

ACPD
10, 25389–25433, 2010

3.2.3 Missclassification of aerosols as clouds

Figure 7 shows five cross sections of the plumes. This haze layer with a high dust component is classified as clouds instead of aerosols in the CALIOP level 2 daytime products (panel a, b, d), but it is correctly classified as aerosols in the nighttime retrievals (panels c, e). We believe that the erroneous classification of aerosol into cloud is caused by assumptions in the cloud/aerosol discrimination algorithm at high latitudes. Initially, a feature is classified by the algorithm as cloud or aerosol based on the intensity of attenuated backscatter, color ratio and altitude (Liu et al., 2004). Then, aerosol layers exhibiting an IVDR value in excess of a given threshold are reclassified as clouds and denominated CAD 101 (Liu et al., 2009). The IDVR threshold is latitude-dependent: 0.15 (50–60° N), 0.10 (60–70° N), 0.05 (70–82° N). The procedure was implemented to reduce misclassification of cirrus clouds and ice-crystal precipitation as aerosols (Liu et al., 2009). This type of precipitation, also called diamond dust, displays optical properties very similar to those of dust (Bourdages et al., 2009). It appears that this assumption leads to the misclassification of dust over the Arctic as clouds especially for daytime retrievals but also for some nighttime retrievals. As a result, in our case study the same coherent aerosol feature was classified as either aerosol or cloud solely depending on its latitude. This is illustrated in panel e of Fig. 7, where poleward of 70° N the aerosol feature is classified as cloud.

The mean IVDR of most plume cross section is greater than 0.05, which corresponds to the IVDR threshold for features retrieved poleward of 70° N (Table 2). Values of IVDR in the range 0.02–0.09 are common for winter/spring Arctic aerosols (Ishii et al., 2001). The aerosol plume was centered north of 70° latitude at nearly all times it was observed by CALIOP during 12–19 March period, and therefore the majority of aerosol layers were misclassified as "cloud CAD 101". When we segregate the retrievals by day and night we observe that the misclassification is more frequent under daytime conditions (69% of the layers) than under nighttime conditions (32% of the layers are misclassified). The misclassified aerosol layer backtrajectories follow very closely the

ACPD
10, 25389–25433, 2010

backtrajectories associated with correctly classified layers. CloudSat satellite observations do not detect any condensed water phase corresponding to the CAD 101 cloud layers (not shown), also confirming the misclassification.

As we were completing this study, a new version of the classification algorithm has been released, version 3.01, which does not employ the CAD 101 but incorporates latitude and depolarization ratio into a five dimensional probability density function (Liu et al., 2010). With respect to the specific case study under examination, the new algorithm generally performs better under nighttime conditions. However, daytime misclassification of aerosol layers as clouds persists.

3.2.4 Comparison between observed and modeled haze layers

There is good agreement between GEOS-Chem and CALIOP on the horizontal and vertical location of the plume (Figs. 5 and 7). The model shows that dust accounts for 20% of the AOD of this haze event. This is somewhat lower than expected based on the high IDVR observed by CALIPSO. The model likely underestimates the dust AOD in this case. Only a small fraction of the aerosol mass that had accumulated over the Sea of Japan and Eastern China was exported to the Arctic. The aerosol pool located over the Sea of Japan is highly spatially and temporally inhomogeneous: the AERONET station in Osaka in southern Sea of Japan records large spikes in coarse mode fraction that occur on hourly time scales on 10 March, 2007. The model thus probably does not capture the strong spatial aerosol inhomogeneity of this complex event.

Because of the CALIOP misclassification, we used a different approach to quantitatively compare model and observation, relying on Level-1 profile data. We selected all cloud free regions of the plumes listed in Table 2, at least 320 km long. We then averaged the attenuated backscatter profiles horizontally and smoothed them with a running mean. We subtracted the molecular attenuated backscatter from the measured attenuated profile, to obtain the particulate attenuated backscatter profile assuming a lidar ratio (ratio of extinction to backscatter coefficients) of 50 sr and using the definition

ACPD
10, 25389–25433, 2010

of attenuated backscatter of Vaughan et al. (2004). This profile could then be compared with GEOS-Chem profile of attenuated backscatter obtained by using the Beer-Lambert law to attenuate the backscatter coefficient from the various species. In order to convert modeled extinction profiles into backscatter profiles we used lidar ratios of 70 sr for sulfate, black carbon, organic carbon, 40 sr for dust aerosols and 20 sr for sea salt (Winker et al., 2009).

The resulting attenuated aerosol backscatter (β'), integrated over the altitude interval where CALIOP observes the plume, are 1.21 ± 0.60 for CALIOP and 0.73 ± 0.25 for GEOS-Chem (Table 2). The model β' is lower than observations by ~40%, possibly due to the underestimate of the dust component.

3.3 20–27 October export episode

This episode occurred in mid-autumn, a season that is not typically associated with elevated Arctic Haze levels. This is the time of the year when the Siberian anticyclone begins to build up at the end of the Monsoon season.

3.3.1 Morphology and optical properties of the observed haze layers

Figure 8 shows the location of the observed layers and their associated backtrajectories. The first plume cross section was observed above the northeastern Siberian sector of the Arctic. Part of the plume then traveled across the Arctic Ocean and it was last observed by CALIOP on 27 October near the Canadian islands of the Northwest Territories.

Table S1 in the Supplement gives a quantitative characterization of the 21 cross sections observed. CALIOP indicates thin layers with average thickness of 1 km, with a few instances of 2–4 km thick layers. The aerosol plume is initially observed at altitudes of 3–5 km but subsides to 2–3.5 km after 25 October. Values of IVDR and color ratio are very similar to those of the February case study, indicating pollution aerosols and low dust levels.

ACPD
10, 25389–25433, 2010

3.3.2 Meteorology

Figure 9 illustrates the synoptic situation during the export event. The ascent is associated with the early development of a mid-latitude cyclone triggered by a deep trough in the middle troposphere. A low-pressure center is seen at the surface on 17 October 2007 in the lee of the Yablonovyy mountain range, near the border between northeastern China and Russia (L in Fig. 9, right panels). The build-up of the polluted airmass in the source area was favored by weak surface winds and anticyclonic conditions during the two days preceding the onset of the export. The aerosols were lifted up to the free troposphere and were carried northward along the downstream ridge. The backtrajectories (Fig. 8) indicate that the origin of the aerosols is NE China, with only 4% of trajectories coming from the Gobi desert. The transport was characterized by elevated relative humidities, consistent with the presence of clouds. Precipitation occurred during most of the transport, until 23 October and more sporadically afterwards. After 25 October the plume began to subside and relative humidity dropped sharply. Subsidence followed the spatially inhomogeneous pattern of low and high pressure systems over the Arctic. Throughout the whole period when the plume was observed, back trajectories also indicate a steady cooling in potential temperature of ∼1.5 °C/day, similar to the cooling rate recorded for the springtime export events.

3.3.3 Comparison between observed and modeled haze layers

Figure 10 shows five plume cross sections observed during this event. Ice clouds are often observed within the aerosol enhancement (panels b, c in Fig. 10). The model generally reproduces the location and altitude of the aerosol layers throughout the 10-day duration of the event. Panels d, e of Fig. 10 illustrate how, even 9–10 days after the export began, the model is able to reproduce the thin aerosol layers in the Beaufort Sea, although in the last case the magnitude of the subsidence undergone by the plume seems to be underestimated. GEOS-Chem underestimates the observed extinction in the plumes (model AOD=0.022, observed AOD=0.038, Table S1). Better

ACPD
10, 25389–25433, 2010

agreement is found for the 0–10 km AOD (0.055 vs. 0.043), indicating that the model spreads out the aerosols in the vertical.

4 Discussion

In all three export events documented here, the initial phase of the transport is strongly meridional, confined between 120° E–180° E, with a weak or absent zonal component. Transport was rapid (3–4 days to reach the Arctic) and precipitation took place predominantly in the initial phase of the export near the source region. These characteristics are consistent with the rapid transport pathway from East Asia described in Stohl (2006). Once in the Arctic, plumes generally travel slowly due to the weak temperature gradients that cause the free troposphere westerlies to slow down, and often migrate toward the northeast.

The dominant aerosol component in the plumes is sulfate in all cases, representing ~80% of the extinction. Park et al. (2005) used aircraft observations in Asian outflow to derive an export efficiency of SO_x (SO_4^{2-}+SO_2) of 0.06–0.21 at 4–6 km altitude. This efficient scavenging was due to wet processes associated with warm conveyor belts and convection, and the observed values were reproduced by GEOS-Chem. This scavenging efficiency is comparable to the ratio between the plume AOD over the Arctic (0.02–0.10) and the AOD over the source region prior to the export (0.40–1.10), which gives a rough indication of the ratio between the aerosols mass that survived scavenging to the aerosols mass in the boundary layer prior to the export.

Our case studies illustrate that in order for an asian airmass to travel to the Arctic two conditions must be satisfied: (1) a lifting mechanism has to be present and, (2) a favorable synoptic pattern leading to meridional transport must exist and persist for a period of at least 3–7 days. Here, the lifting mechanism is associated with a low-pressure center accompanying the genesis or decay of a mid-latitude cyclone. Late winter and spring are the most active cyclogenesis periods in East Asia. NE China, where all three events originated, is at the cross road of the storm tracks that originate

ACPD
10, 25389–25433, 2010

in the lee of the Altai-Sayan mountains and along the East Asian coastline (Chen et al., 1991). The meridional transport from Asia is also expected to maximize in winter/spring due to the annual maximum in the frequency of occurrence of blocking patterns in the 120° E–150° E longitude band (Barriopedro et al., 2005). Similarly, blocking patterns frequently occur during winter/spring in the 20–50° E region, favoring meridional export from Europe to the Arctic (Lejenas and Økland, 1983; Raatz and Shaw, 1984).

Figure 11 illustrates the 500 hPa geopotential height anomalies (left panels) and sea level pressure anomalies (right panels) corresponding to the first three days of transport for each case study examined here. The most evident feature is the anomalous high located in the NW Pacific, common to all three episodes. Often associated with it is a negative anomaly centered over Eastern Siberia or Northern China. The anomaly pattern for the two spring case studies shows a clear blocking configuration. The October case study displays a trough-ridge configuration. The lifting mechanism, which can simply be a weak low pressure center with little upper air signature, is not always apparent on these anomalies. By inspection of the CALIOP 2008 and 2009 observations, we identified eight additional Asian export events (five in March and three in December). These events all display a similar 500 hPa geopotential height anomaly, with either a blocking pattern or a trough-ridge configuration favoring poleward transport. By compositing all 11 events, we find a clear east-west dipole pattern (Fig. 11, bottom panel).

We examine next the relationship between enhanced Asian export to the Arctic and teleconnection patterns. The two main Northern Hemisphere indices that might be relevant to our study are the Western Pacific (WP) and the Pacific North American (PNA) indices. The PNA emerges in the form of a quadripole (Wallace and Gutzler, 1981) but can be alternatively defined as the projection of the second mode of northern hemisphere variability in a rotated EOF analysis of 500 hPa mean monthly anomalies onto the daily 500 hPa anomaly (http://www.ncdc.noaa.gov/teleconnections/pna/). Strong blocking activity in the central North Pacific characterizes the negative phase. The WP manifests itself as a north-south oriented anomaly dipole in 500 hPa geopotential

ACPD
10, 25389–25433, 2010

heights, with centers of actions located along 155° E at 60° N and 30° N (Wallace and Gutzler, 1981). It is less broad than the PNA but it also relates to blocking frequency in the Western Pacific (Barriopedro et al., 2005). Daily values of the WP index were calculated from the definition of Wallace and Gutzler (1981), though the sign is inverted since we adopt the most common sign convention that defines a positive polarity when negative anomalies are present in the NW Pacific and positive anomalies are found to its south. We obtained daily values of the PNA index from the Climate Prediction Center of the National Weather Service (http://www.cpc.noaa.gov/products/precip/CWlink/daily_ao_index/history/history.shtml).

Table 3 summarizes the sign of WP and PNA during the initial stage of export for the eleven major episodes observed by CALIOP in 2007–2009. The WP index is negative in 5 out of 11 episodes, with near zero or positive values in the remaining 6 episodes. The PNA index is negative during 4 out of 11 events.

In order to evaluate how accurately the highlighted synoptic mechanisms explain pollution episodes from East Asia we define an empirical index based on a composite of the 500 hPa geopotential height anomaly pattern of the 11 cases of Table 3. This index, which we call the Asian Meridional Export (AME) index, is defined as the difference of the 500 hPa geopotential height anomalies at 160° E, 47.5° N and 120° E, 60° N. These two points correspond to the two poles of action identified in the composite anomaly for all 11 events (Fig. 11, bottom panel). The 7-day smoothed time-series of the AME index as well as WP and PNA indices are shown in the top panel of Fig. 12. The bottom panel of Fig. 12 shows a 3-year timeseries of the model Asian anthropogenic sulfate AOD at 70° N averaged between 120° E and 180° E. Winter and early spring episodes are dominated by sulfate, whereas the period March–August is characterized by peaks in dust associated with dust storms (Shao and Dong, 2006). Strongly positive values of AME occurred in mid-February to mid-March 2007, March and April of 2008, November–December 2008, February–March 2009 and October–November 2009. All 11 events are associated with positive daily values of AME (Table 3).

ACPD
10, 25389–25433, 2010

Table 4 summarizes the correlations between the WP, PNA and AME indices and the anthropogenic Asian sulfate AOD for 2007–2009. We choose the sulfate AOD in place of the total AOD because the latter is strongly influenced by dust storms that originate in remote regions, resulting in poor correlations between sulfate and dust AOD (Fig. 12, bottom panel). During winter and spring the AME index is strongly correlated with the anthropogenic Asian timeseries ($r = 0.76$ and $r = 0.63$, significant at 95% confidence level, respectively). The WP and PNA indices display lower correlation coefficients. The correlation of AME with the Asian anthropogenic timeseries peaks at a lag of 2 days which corresponds to the transport time from the mid-latitudes to 70° N. Correlations for all 3 indices become weaker in summer and autumn (Table 4). The strength and persistence of meridional transport, as measured by AME, captures 40–60% of the variance in the modeled Asian anthropogenic AOD at 70° N in winter/spring and thus appears to be a good predictor of export of Asian pollution to the Arctic.

5 Conclusions

We used direct aerosol plume observation from the space borne lidar onboard CALIPSO satellite together with 3-D chemical transport model simulations driven by assimilated meteorological fields, and lagrangian backtrajectories to follow the evolution of three aerosol plumes over the Arctic that originated in East Asia in 2007. Two of the export episodes took place in early spring, the time when Arctic Haze is at its climatological peak, whereas the third occurred in autumn. Haze layers were detected at altitudes of 2–8 km, exhibited a poleward tilt following potential temperature surfaces. Individual layers had a mean thickness of ~1500 m. We find good agreement between model simulations and observations as to the geographical location, thickness, and altitude of the haze layers.

The mean observed optical depth of aerosol layers was 0.04 (cases 1 and 3) with depolarization ratio consistently around 0.03; in the second springtime case the AOD was not available due to the misclassification of aerosols as clouds. In this case, we

ACPD
10, 25389–25433, 2010

find a mean integrated attenuated backscatter of 1.21×10^{-3} sr^{-1}, and higher values of the depolarization ratio, in the 0.05–0.07 range. Values of color ratio are found to be mostly between 0.2 and 0.3 in all cases.

In all three cases examined here, the dominant source for the aerosol layers is NE China. In 5–10% of the individual aerosols layers, backtrajectories indicate an origin in the Gobi desert. Pollutants accumulate in the shallow boundary layer and are ventilated by the passage of a cold surge, represented by a developing cyclone or a waning cyclone approaching from the west. The polluted airmass ascends rapidly ahead of the cold front and significant precipitation takes place in these early stages of transport. In order for rapid transport to take place, the upper level field has to be strongly meridionally oriented in association with two separate patterns. We noted that this occurs in two situations: the first is the presence of a blocking high in the western Pacific (dominating in the spring cases); the second is a pronounced ridge just downstream of a surface low (autumn case).

Backtrajectories confirm that once the ascent is complete, potential temperature slowly but steadily decreases at a rate of ~1.5 °C/day. Subsidence accompanies this radiative cooling, although it takes place less gradually. No plume was observed to reach the surface.

In the export episode that took place in March, the CALIOP layer classification algorithm misclassifies a large number of aerosol layers as clouds. The misclassification occurs because the layers are relatively depolarizing due to the presence of dust which is interpreted as ice crystals by the algorithm. The misclassification is more pronounced for daytime than nighttime retrievals due to positive bias in the daytime depolarization ratio values measured at daytime. In the case of this export event, 10% of backtrajectories can be tracked to the Gobi desert, twice as many as in the two other cases documented.

We examined the relationship of the Western Pacific and Pacific North American indices to the frequency of occurrence of major aerosol export episodes from East Asia. Major export episodes observed by CALIOP were contrasted with a timeseries

ACPD
10, 25389–25433, 2010

of anthropogenic Asian sulfate AOD at 70° N across the corridor of dominant transport (120° E to 180° E). Both WP and PNA exhibit a weak tendency toward negative values during enhanced Arctic export events.

We defined an empirical index, named Arctic Meridional Export (AME) based on a composite of the anomaly pattern of 500 hPa heights of nine major export events in 2007–2009. AME correlates well with enhanced export of Asian pollution to the Arctic during winter ($r = 0.76$) and spring ($r = 0.63$). In comparison PNA and WP display a lower correlation ($r = -0.35$ and $r = -0.08$, respectively, in the spring)

CALIOP measurements provide a potential method of resolving the discrepancies among CTMs in that it can provide constraints on the vertical location and amount of aerosols transported to the Arctic. The model calculated plume AOD and backscatter fall within the uncertainties range of the CALIOP measurements (±40%). The sharper boundaries of the aerosol layers observed by CALIOP are partly a result of the altitude dependent sensitivity of the instrument. The CALIOP detection accuracy however is sensitive to the illumination conditions which affect the signal-to-noise ratio. Our case studies took place under favorable conditions for retrievals, since the transport was rapid (and consequently the plumes underwent little dilution), and occurred mainly at nighttime. As the sun rises over the Arctic it becomes more problematic to detect faint pollution aerosol plumes transported over long distances and to track them over time. This aspect has to be carefully considered if one aims at constructing a satellite-based long-term climatology of the vertical distribution of haze layers over the Arctic.

Supplementary material related to this article is available online at: http://www.atmos-chem-phys-discuss.net/10/25389/2010/acpd-10-25389-2010-supplement.zip.

Acknowledgements. This work was supported by funding from the National Aeronautic and Space Administration under award NNX08Q07G. We also acknowledge the NASA Langley Research Center Atmospheric Science Data Center for the CALIPSO data. T. L. Anderson acknowledges additional support from the National Science Foundation (grant # ATM-0601177).

ACPD

10, 25389–25433, 2010

References

Alexander, B., Savarino, J., Lee, C. C. W., Park, R. J., Jacob, D. J., Thiemens, M. H., Li, Q. B., and Yantosca, R. M.: Sulfate formation in sea-salt aerosols: Constraints from oxygen isotopes, J. Geophys. Res., 110, D10307, doi:10.1029/2004JD005659, 2005.

Barriopedro, D., Garcia-Herrera, R., Lupo, A., and Hernandez, E.: A climatology of Northern Hemisphere Blocking, J. Climate, 19, 1042–1063, 2005.

Bey, I., Jacob, D. J., Yantosca, R. M., Logan, J. A., Field, B. D., Fiore, A. M., Li, Q., Liu, H. Y., Mickley, L. J., and Schultz, M. G.: Global modeling of tropospheric chemistry with assimilated meteorology: Model description and evaluation, J. Geophys. Res., 106(D19), 23073–23095, 2001.

Bourdages, L., Duck, T. J., Lesins, G., Drummond, J. R., and Eloranta, E. W.: Physical properties of High Arctic tropospheric particles during winter, Atmos. Chem. Phys., 9, 6881–6897, doi:10.5194/acp-9-6881-2009, 2009.

Carlson, T. N.: Speculations on the movement of polluted air to the Arctic, Atmos. Environ., 15(8), 1473–1477, 1981.

Chen, S.-J., Kuo, Y.-H., Zhang, P.-Z. and Bai, Q.-F.: Synoptic Climatology of Cyclogenesis over East Asia, 1958–1987, Am. Meteor. Soc., 119, 1407–1418, 1991.

Curry, J.: On the formation of continental polar air, Am. Meteor. Soc., 40, 2278–2292, 1983.

Draxler, R. R. and Hess, G. D.: Description of the HYSPLIT_4 Modeling System, NOAA Technical Memorandum ERL ARL-224, revised January 2004.

Fairlie, T. D., Jacob, D. J., and Park, R. J.: The impact of transpacific transport of mineral dust in the United States, Atmos. Environ., 41, 1251–1266, 2007.

Ishii, S., Shibata, T., Sakai, T., Kido, M., Hara, K., Osada, K., Iwasaka, Y., Nagai, T., Fujimoto, T., Itabe, T., Mizutani, K., and Uchino, O.: The source, size and chemical composition of the winter Arctic tropospheric aerosol layer observed by lidar at Eureka, Canada, J. Meteorol. Soc. Jpn., 79(1), 61–78, 2001.

Iversen, T. and Joranger, E.: Arctic air pollution and large-scale atmospheric flows, Atmos. Environ., 19(12), 2099–2108, 1985.

Kalnay, E. and Coauthors: The NCEP/NCAR Reanalysis 40-year Project, B. Am. Meteor. Soc., 77, 437–471, 1996.

Klonecki, A., Hess, P., Emmons, L., Smith, L., Orlando, J., and Blake, D.: Seasonal changes in the transport of pollutants into the Arctic troposphere-model study, J. Geophys. Res.,

ACPD
10, 25389–25433, 2010

108(D4), 8367, doi:10.1029/2002JD002199, 2003.
Koch, D. and Hansen, J.: Distant origins of Arctic black carbon: A Goddard Institute for Space Studies ModelE experiment, J. Geophys. Res., 110, D04204, doi:10.1029/2004JD005296, 2005.
Lejenas, H. and Økland, H.: Characteristics of northern hemisphere blocking as determined from a long time series of observational data, Tellus, 35A, 350–362, 1983.
Liao, H., Seinfeld, J., Wu, S., and Mickley, L.: Biogenic Secondary Organic Aerosol over the United States: Comparison of Climatological Simulations with Observations, J. Geophys. Res, 112, D06201, doi:10.1029/2006JD007813, 2007.
Liu, D., Wang, Z., Liu, Z., Winker, D., and Trepte, C.: A height resolved global view of dust aerosols from the first year CALIPSO lidar measurements, J. Geophys. Res., 113, D16214, doi:10.1029/2007JD009776, 2008.
Liu, Z., Vaughan, M. A., Winker, D. M., Hostetler, C. A., Poole, L. R., Hlavka, D., Hart, W., and McGill, M.: Use of probability distribution functions for discriminating between cloud and aerosol in lidar backscatter data, J. Geophys. Res., 109, D15202, doi:10.1029/2004JD004732, 2004.
Liu, Z., Vaughan, M. A., Winker, D. M., Kittaka, C., Kuehn, R. E., Getzewich, B. J., Trepte, C. R., and Hostetler, C. A.: The CALIPSO Lidar Cloud and Aerosol Discrimination: Version 2 Algorithm and Initial Assessment of Performance, J. Atmos. Ocean. Tech., 26, 1198–1213, doi:10.1175/2009JTECHA1229.1, 2009.
Liu, Z., Kuehn, R., Vaughan, M., Winker, D., Omar, A., Powell, K., Trepte, C., Hu, Y., and Hostetler, C.: The CALIPSO Cloud And Aerosol Discrimination: Version 3 Algorithm and Test Results, 25th International Laser Radar Conference (ILRC), St. Petersburg, Russia, 2010.
Martin, R. V., Jacob, D. J., Yantosca, R. M., Chin, M., and Ginoux, P.: Global and regional decreases in tropospheric oxidants from photochemical effects of aerosols, J. Geophys. Res., 108, 4097, doi:10.1029/2002JD002622, 2003.
Mitchell, M.: Visual range in the polar regions with particular reference to the Alaskan Arctic, J. Atmos. Terr. Phys., Special Supplement, 195–211, 1956.
Olivier, J. G. J. and Berdowski, J. J. M.: Global emissions sources and sinks, in: The Climate System, edited by: Berdowski, J., Guicherit, R., and Heij, B. J., A.A. Balkema Publishers/Swets & Zeitlinger Publishers, Lisse, The Netherlands, ISBN 90 5809 255 0, 33–78, 2001.

ACPD
10, 25389–25433, 2010

Park, R. J., Jacob, D. J., Chin, M., and Martin, R. V.: Sources of carbonaceous aerosols over the United States and implications for natural visibility, J. Geophys. Res., 108(D12), 4355, doi:10.129/2002JD003190, 2003.
Park, R. J., Jacob, D. J., Field, B. D., Yantosca, R. M., and Chin, M.: Natural and transboundary pollution influences on sulfate-nitrate-ammonium aerosols in the United States: implications for policy, J. Geophys. Res., 109, D15204, doi:10.1029/2003JD004473, 2004.
Park, R. J., Jacob, D. J., Palmer, P. I., Clarke, A. D., Weber, R. J., Zondlo, M. A., Eisele, F. L., Bandy, A. R., Thornton, D. C., Sachse, G. W., Bond, T. C.: Export efficiency of black carbon aerosol in continental outflow: Global implications, J. Geophys. Res., 110, D11205, doi:10.1029/2004JD005432, 2005.
Quinn, P. K., Miller, T. L., Bates, T. S., Ogren, J. A., Andrews, E., and Shaw, G. E.: A three year record of simultaneously measured aerosol chemical and optical properties at Barrow, Alaska, J. Geophys. Res., 107(D11), 4130, doi:10.129/2001JD001248, 2002.
Raatz, W. E. and Shaw, G. E.: Long-range tropospheric transport of pollution aerosols into the Alaskan Arctic, J. Clim. Appl. Met., 23, 1052–1064, 1984.
Rastigejev, Y., Park, R., Brenner, M. P., and Jacob, D. J.: Resolving intercontinental pollution plumes in global models of atmospheric transport, J. Geophys. Res., 115, D02302, doi:10.1029/2009JD012568, 2010.
Shao, Y. and Dong, C. H.: A review on East Asian dust storm climate, modeling and monitoring, Glob. Planet. Change, 52, 1–22, 2006.
Shaw, G. E.: The Arctic Haze phenomenon, B. Am. Meteorol. Soc., 76, 2403–2413, 1995.
Shindell, D. T., Chin, M., Dentener, F., Doherty, R. M., Faluvegi, G., Fiore, A. M., Hess, P., Koch, D. M., MacKenzie, I. A., Sanderson, M. G., Schultz, M. G., Schulz, M., Stevenson, D. S., Teich, H., Textor, C., Wild, O., Bergmann, D. J., Bey, I., Bian, H., Cuvelier, C., Duncan, B. N., Folberth, G., Horowitz, L. W., Jonson, J., Kaminski, J. W., Marmer, E., Park, R., Pringle, K. J., Schroeder, S., Szopa, S., Takemura, T., Zeng, G., Keating, T. J., and Zuber, A.: A multi-model assessment of pollution transport to the Arctic, Atmos. Chem. Phys., 8, 5353–5372, doi:10.5194/acp-8-5353-2008, 2008.
Stohl, A.: Characteristics of atmospheric transport into the Arctic troposphere, J. Geophys. Res., 111, D11306, doi:10.129/2005JD006888, 2006.
van der Werf, G. R., Randerson, J. T., Giglio, L., Collatz, G. J., Kasibhatla, P. S., and Arellano Jr., A. F.: Interannual variability in global biomass burning emissions from 1997 to 2004, Atmos. Chem. Phys., 6, 3423–3441, doi:10.5194/acp-6-3423-2006, 2006.

ACPD
10, 25389–25433, 2010

Vaughan, M., Young, S., Winker, D., Powell, K., Omar, A., Liu, Z., Hu, Y. and Hostetler, C.: Fully automated analysis of space-based lidar data: an overview of the CALIPSO retrieval algorithms and data products, Proc. SPIE, 5575, 16–30, doi:10.1117/12.572024, 2004.

Wallace, J. M. and Gutzler, D. S.: Teleconnections in the Geopotential Height Field during the Northern Hemisphere Winter, Mon. Weather Rev., 109, 784–812, 1981.

Winker D. M., Hunt, W., and Hostetler, C.: Status and performance of the CALIOP lidar, Proc. SPIE Int. Soc. Opt. Eng., 5575, 8–15, 2004.

Winker, D. M., Vaughan, M. A., Omar, A., Hu, Y., and Powell, J. A.: Overview of the CALIPSO Mission and CALIOP Data Processing Algorithms, J. Atmos. Ocean. Tech., 26, 2310–2323, doi:10.1175/2009JTECHA1281.1, 2009.

Young, S. A. and Vaughan, M. A.: The retrieval of profiles of particulate extinction from Cloud Aerosol Lidar Infrared Pathfinder Satellite Observations (CALIPSO) data: Algorithm description, J. Atmos. Ocean. Technol., 26, 1105–1119, doi:10.1175/2008JTECHA1221.1., 2009.

Zender, C. S., Bian, H., and Newman, D.: The mineral dust entrainment and deposition (DEAD) model: description and 1990s dust climatology, J. Geophys. Res, 108(D14), 4416, doi:10.1029/2002JD002775, 2003.

Zhang, Q., Streets, D. G., Carmichael, G. R., He, K. B., Huo, H., Kannari, A., Klimont, Z., Park, I. S., Reddy, S., Fu, J. S., Chen, D., Duan, L., Lei, Y., Wang, L. T., and Yao, Z. L.: Asian emissions in 2006 for the NASA INTEX-B mission, Atmos. Chem. Phys., 9, 5131–5153, doi:10.5194/acp-9-5131-2009, 2009.

ACPD

10, 25389–25433, 2010

Table 1. Summary of the 23 Arctic aerosol layers observed by CALIOP for the 28 February–4 March 2007 case study.

Date[a]	Location of endpoints (Latitude; Longitude)	Length (km)	CALIOP Mean Altitude (km)	CALIOP IVDR[b]	CALIOP Color Ratio	CALIOP AOD (plume|column)[c]	GEOS-Chem AOD w/o TH[d] (plume|column)	GEOS-Chem AOD w/ TH[d] (plume|column)
02-28 17.33 N	72.5° N;148.8° E|80.9° N;174.0° W	1275	3.8	0.027	0.26	0.04|0.07	0.09|0.13	0.07|0.09
02-28 19.12 N	79.3° N;146.7° E|81.8° N;175.7° W	720	5.3	0.029	0.26	0.05|0.06	0.04|0.10	0.03|0.06
02-28 19.59 D[e]	80.9° N;169.8° W|81.8° N;161.9° E	475	5.7	0.031	0.36	0.05|0.05	0.02|0.08	0.02|0.04
02-28 20.51 N[e]	81.4° N;145.3° E|81.8° N;161.9° E	235	5.2	0.032	0.29	0.03|0.03	0.05|0.12	0.05|0.07
02-28 21.37 D	77.1° N;169.6° W|81.8° N;141.8° E	1065	5.1	0.028	0.32	0.03|0.03	0.06|0.12	0.06|0.07
02-28 23.16 D	64.5° N;172.1° W|67.9° N;175.5° W	400	3.7	0.065	0.34	0.01|0.01	0.01|0.08	0.01|0.03
02-28 23.16 D	75.2° N;171.8° E|80.1° N;148.3° E	765	3.7	0.021	0.31	0.04|0.05	0.06|0.12	0.06|0.08
03-01 13.20 N	60.1° N;161.5° W|75.3° N;141.6° W	1845	4.0	0.044	0.27	0.08|0.08	0.07|0.11	0.06|0.07
03-01 14.59 N	75.2° N;166.5° W|79.1° N;151.1° W	560	4.3	0.024	0.24	0.03|0.03	0.05|0.10	0.04|0.06
03-01 16.38 N	74.6° N;167.2° E|81.3° N;153.9° W	1120	3.6	0.026	0.24	0.02|0.03	0.07|0.11	0.05|0.06
03-01 18.17 N	76.9° N;149.4° E|81.8° N;164.4° W	1040	4.1	0.024	0.25	0.02|0.03	0.06|0.11	0.05|0.07
03-02 12.24 N	63.1° N;145.3° W|74.9° N;128.7° W	1440	4.0	0.025	0.22	0.03|0.03	0.04|0.08	0.03|0.03
03-02 14.03 N	54.1° N;175.7° W|63.1° N;170.1° W	1040	2.1	0.052	0.28	0.09|0.11	0.03|0.09	0.01|0.05
03-02 15.42 N	75.5° N;176.5° W|79.8° N;156.7° W	660	3.5	0.028	0.26	0.02|0.06	0.06|0.09	0.04|0.05
03-02 17.21 N	77.2° N;164.2° E|80.8° N;171.6° W	640	3.5	0.027	0.27	0.03|0.04	0.05|0.10	0.04|0.05
03-03 11.29 N	64.1° N;130.6° W|71.0° N;122.7° W	820	3.6	0.029	0.26	0.04|0.05	0.04|0.07	0.02|0.03
03-03 13.08 N	71.6° N;146.4° W|74.3° N;141.0° W	340	3.4	0.019	0.21	0.02|0.05	0.04|0.09	0.04|0.05
03-03 14.47 N	72.3° N;169.8° W|77.6° N;155.6° W	700	3.1	0.020	0.21	0.01| 0.01	0.04|0.08	0.02|0.03
03-03 16.26 N	77.4° N;179.1° E|80.3° N;163.8° W	480	3.5	0.026	0.29	0.01|0.01	0.03|0.08	0.02|0.03
03-03 18.05 N	80.2° N;171.4° E|80.9° N;179.2° E	160	3.3	0.029	0.23	0.02|0.02	0.01|0.08	0.00|0.03
03-03 20.30 D	78.7° N;159.7° W|80.4° N;172.5° W	320	3.6	0.032	0.29	0.02|0.02	0.02|0.07	0.01|0.02
03-03 22.09 D	71.7° N;163.8° W|77.1° N;177.5° W	720	2.8	0.010	0.24	0.01|0.01	0.03|0.07	0.02|0.03
03-04 10.33 N	61.0° N;119.1° W|65.8° N;115.2° W	560	3.9	0.029	0.22	0.05|0.06	0.04|0.07	0.02|0.02
03-04 15.30 N	77.7° N;165.9° W|78.7° N;160.9° W	160	2.9	0.026	0.27	0.02|0.02	0.03|0.06	0.00|0.00
Mean[f]	–	730	3.8	0.030±0.011	0.26±0.04	0.038|0.046	0.050|0.097	0.038|0.053

[a] Dates are given as MM-DD UTC time (hh:mm). N or D indicates night or day observation.

[b] Integrated Volume Depolarization Ratio (IVDR).

[c] The first number corresponds to the observed AOD in the plume only while the second number indicates the AOD for the entire column (0–10 km).

[d] The two GEOS-Chem columns correspond to the AOD without threshold (*w/o* TH) and with threshold (*w*/TH) based on the CALIOP sensitivity.

[e] The third haze layer was observed under daytime and nighttime conditions so it straddles 2 files.

[f] All mean aerosol properties are weighted by the length of the cross-section.

ACPD
10, 25389–25433, 2010

Table 2. Summary of the 37 Arctic aerosol layers observed by CALIOP during the 12–19 March export event. Refer to Table 1 for the legend.

Date	Location of endpoints (Latitude; Longitude)	Length (km)	Mean Altitude (km)	CALIOP IVDR	Color Ratio	Int. β'^{a} ($\times 10^{-3}$ sr^{-1})	GEOS-Chem Int. β'^{a} ($\times 10^{-3}$ sr^{-1})
03-12 17.59 N	64.5° N;132.3° E|71.1° N;140.1° E	800	4.6	0.063	0.29	–	–
03-13 18.43 N	66.8° N;123.7° E|77.4° N;145.1° E	1360	4.0	0.054	0.30	–	–
03-14 00.26 D	76.6° N;150.6° E|80.5° N;128.4° E	640	4.1	0.058	0.31	1.03	0.70
03-14 02.05 D	69.1° N;141.4° E|77.7° N;121.7° E	1120	3.2	0.069	0.36	1.81	0.94
03-14 18.34 D	79.8° N;147.2° E|81.3° N;164.6° E	355	3.9	0.062	0.32	1.77	1.20
03-14 19.26 N	74.2° N;124.3° E|79.6° N;146.0° E	800	4.3	0.053	0.25	–	–
03-14 20.13 D	79.8° N;122.6° E|81.8° N;167.3° E	795	3.0	0.053	0.40	–	–
03-14 21.52 D	79.5° N;175.5° E|81.6° N;121.8° E	960	3.4	0.054	0.34	–	–
03-14 23.30 D	78.0° N;159.0° E|81.7° N;121.2° E	820	3.2	0.077	0.41	–	–
03-15 01.09 D	76.9° N;138.5° E|81.3° N;106.6° E	800	3.9	0.069	0.30	–	–
03-15 17.38 D	79.5° N;159.4° E|80.5° N;129.6° W	1275	4.0	0.049	0.27	0.98	0.91
03-15 19.17 D	80.8° N;146.2° E|81.4° N;167.5° W	770	3.7	0.063	0.34	1.57	0.86
03-15 20.56 D	80.9° N;176.7° E|81.8° N;148.1° E	480	3.4	0.072	0.31	–	–
03-16 01.53 D	81.2° N;97.7° E|81.7° N;63.2° E	560	3.2	0.048	0.29	0.51	0.32
03-16 11.46 D	79.3° N;113.9° W|81.2° N; 95.6° W	395	4.7	0.065	0.29	–	–
03-16 12.39 N	72.9° N;136.4° W|79.1° N;115.2° W	880	3.7	0.047	0.21	0.44	0.83
03-16 13.25 D	79.3° N;139.0° W|81.8° N;93.9° W	835	2.7	0.051	0.41	–	–
03-16 14.17 N	76.3° N;152.6° W|79.1° N;140.3° W	420	3.2	0.047	0.24	–	–
03-16 15.04 D	79.3° N;163.6° W|81.8° N;116.0° W	875	3.6	0.061	0.35	–	–
03-16 16.43 D	80.7° N;118.0° W|81.3° N;167.0° W	820	4.4	0.064	0.34	2.14	0.98
03-16 18.22 D	75.2° N;114.2° W|81.8° N; 165.6° W	1270	4.1	0.073	0.30	2.32	1.10
03-16 20.01 D	76.4° N;142.3° W|80.4° N;163.9° W	640	4.1	0.081	0.31	1.15	0.74
03-17 11.43 N	67.2° N;130.7° W|76.3° N;114.0° W	1140	3.2	0.063	0.26	1.66	0.79
03-17 12.29 D	79.0° N;126.8° W|80.7° N;113.5° W	315	3.9	0.052	0.27	–	–
03-17 13.22 N	69.2° N;153.0° W|78.8° N;127.8° W	1280	3.7	0.046	0.22	0.83	0.68
03-17 14.08 D	79.0° N;151.5° W|81.8° N;115.3° W	715	3.8	0.053	0.26	–	–
03-17 15.47 D	81.6° N;119.7° W|81.8° N;139.9° W	320	3.8	0.065	0.33	–	–
03-17 17.26 D	78.8° N;114.2° W|81.4° N;140.2° W	560	3.8	0.067	0.28	–	–
03-17 19.05 D	71.7° N;117.4° W|77.3° N;131.6° W	740	3.1	0.079	0.28	0.37	0.30
03-17 20.44 D	66.6° N;135.4° W|75.0° N;149.1° W	1040	3.2	0.079	0.34	1.31	0.66
03-18 12.26 N	65.5° N;143.3° W|74.1° N;130.7° W	1060	3.3	0.044	0.21	1.86	0.92
03-18 14.05 N	65.5° N;168.0° W|74.6° N;154.4° W	1115	2.5	0.052	0.26	0.47	0.45
03-18 19.48 D	69.0° N;124.6° W|74.8° N;134.5° W	720	3.1	0.096	0.32	1.13	0.52
03-19 11.31 N	66.4° N;128.5° W|69.1° N;125.4° W	320	3.3	0.045	0.22	0.60	0.55
03-19 11.31 N	72.9° N;119.3° W|76.3° N;110.9° W	440	2.4	0.033	0.18	–	–
03-19 13.10 N	70.2° N;148.6° W|76.1° N;136.1° W	760	3.4	0.045	0.24	–	–
03-19 20.32 D	68.1° N;134.0° W|73.3° N;142.0° W	640	2.2	0.097	0.30	1.03	0.43
Mean[b]	–	780	3.5	0.061±0.014 N:0.051±0.008 D:0.067±0.041	0.30±0.05 N:0.25±0.03 D:0.32±0.04	1.21±0.60	0.73±0.25

[a] Mean attenuated particle backscatter (β') integrated in the plume. β' is given only for cases with clear sky conditions persisting over at least 320 km.

[b] IVDR and color ratio are weighted by the length of the cross-section.

ACPD
10, 25389–25433, 2010

Table 3. Sign of the WP and PNA indices during the early stages of the nine major events observed by CALIOP during the period 2007–2009.

Date[a]	WP[b]	PNA[b]	AME[b]
28 Feb–4 Mar, 2007	–	–	++
12 Mar–19 Mar, 2007	–	~ 0	++
20 Oct–27 Oct, 2007	~ 0	+	+
12 Mar–13 Mar, 2007	~ 0	+	+
14 Mar–17 Mar, 2008	+	~ 0	++
20 Mar–22 Mar, 2008	–	–	++
3 Dec–7 Dec, 2008	–	+	++
15 Dec–18 Dec, 2008	+	~ 0	++
22 Dec–25 Dec, 2008	+	–	++
14 Mar–16 Mar, 2009	~ 0	–	++
20 Mar–27 Mar, 2009	–	~ 0	++

[a] The dates correspond to the times when Arctic haze events are observed by CALIOP.

[b] A double sign indicates absolute values of the index greater than two standard deviation during the 3-day initial phase of export. Near zero values are those whose absolute values within ±0.5 standard deviations.

ACPD
10, 25389–25433, 2010

Table 4. Correlations of WP, PNA and AME index defined in the text with the Asian anthropogenic sulfate AOD at 70° N averaged between 120° E and 180° E.

Seasons	Index[a] WP	PNA	AME
DJF	−0.01	−0.45	**0.76**[b]
MAM	−0.08	−0.35	**0.63**
JJA	−0.19	−0.47	0.07
SON	0.17	−0.17	0.26
Entire timeseries (Dec 2006–Dec 2009)	−0.13	**−0.38**	**0.47**

[a] Timeseries are smoothed with a 7-day running mean. A 2-day lag is applied to all indices.

[b] Values in bold are significant at 95% confidence level.

ACPD
10, 25389–25433, 2010

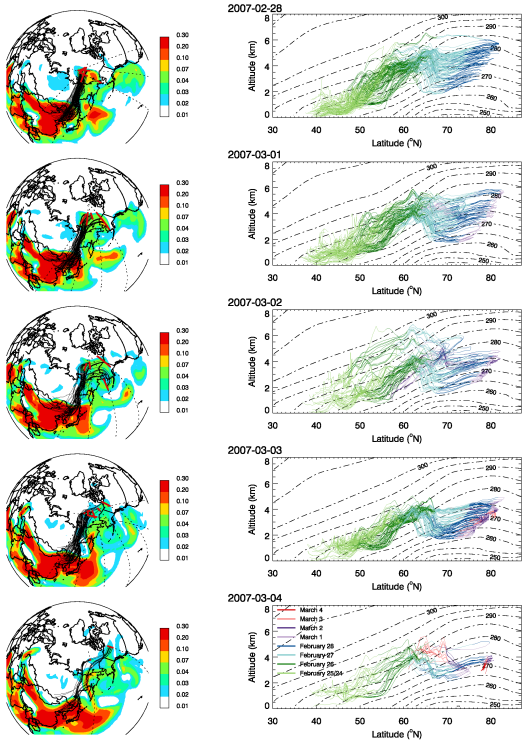

Fig. 1. 28 February–4 March 2007 Arctic haze event. Left column: daily Asian AOD (550 nm) calculated with GEOS-Chem. CALIPSO orbits are indicated by dashed lines and the parts of the orbit where the haze layers are observed are shown in red. Backtrajectories corresponding to the observed aerosol layers are shown in black, starting with 4-day backtrajectories on 28 February, and incremented by 24 h for each subsequent day. Right column: height (altitude above mean sea level) evolution as a function of latitude for backtrajectories shown on the left panel. The backtrajectories are color-coded based on the date (see legend on bottom panel). The potential temperature surfaces (dashed lines) are zonally averaged between 120° E and 150° W and temporally averaged between 25 February, 0Z and the time the last plume was observed for each day.

ACPD
10, 25389–25433, 2010

Satellite observations of aerosol transport from East Asia to the Arctic

M. Di Pierro et al.

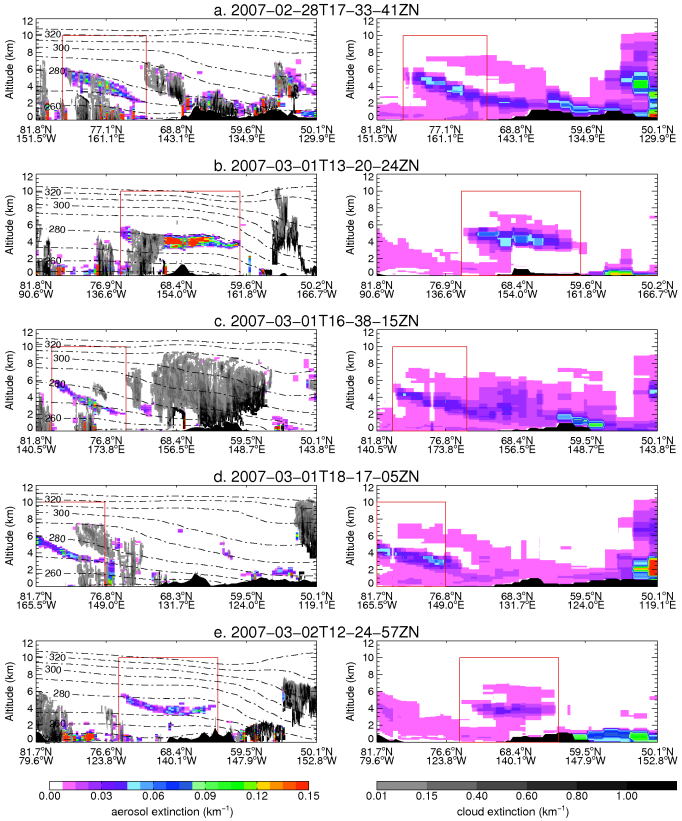

Fig. 2a. Aerosol extinction comparison between CALIOP (L2 profile data, left) and GEOS-Chem (right). Five scenes were chosen among the 23 East Asian plumes observed by CALIOP during the 28 February–4 March period. Aerosol extinctions are plotted in color and cloud extinctions observed by CALIPSO are in gray. The red box delimits the aerosol layers that have an East Asian origin (see text). Potential temperature contours are shown with dashed-dotted lines on the left panels. The text on top of each panel is the CALIOP file identifier.

ACPD
10, 25389–25433, 2010

Satellite observations of aerosol transport from East Asia to the Arctic

M. Di Pierro et al.

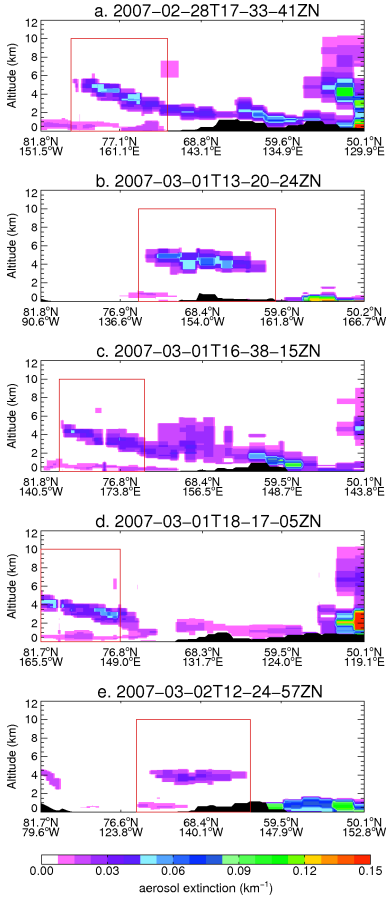

Fig. 2b. Same GEOS-Chem aerosol extinction as Fig. 2a right panels but using the CALIOP nighttime altitude-dependent backscatter sensitivity threshold (see text).

ACPD
10, 25389–25433, 2010

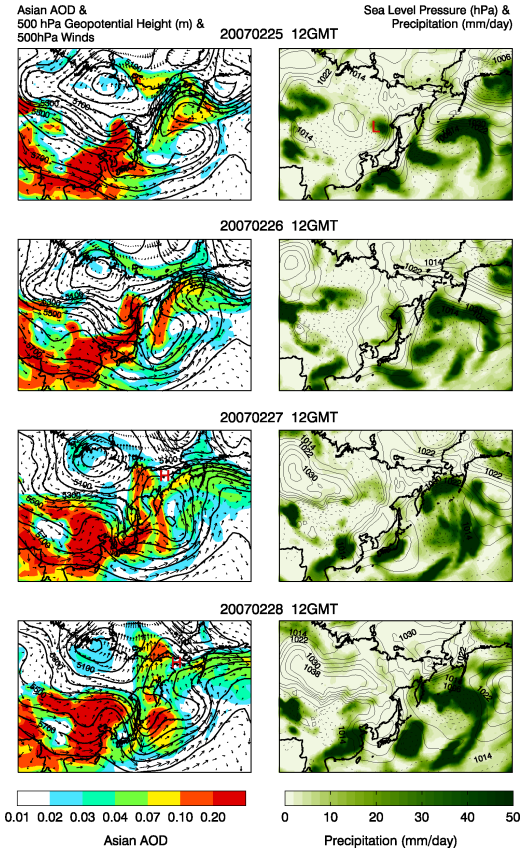

Fig. 3. Left panel: 500 hPa geopotential height (black contours) and corresponding wind vector evolution during the initial period of aerosol export, together with GEOS-Chem Asian AOD (in color) for 25–28 February, 2007. Right panel: sea level pressure (contours) and precipitation (green). SLP contours (4 hPa) are dashed when SLP is below 1014 hPa. H indicates the blocking high pressure system; L shows the location of the low pressure center.

ACPD
10, 25389–25433, 2010

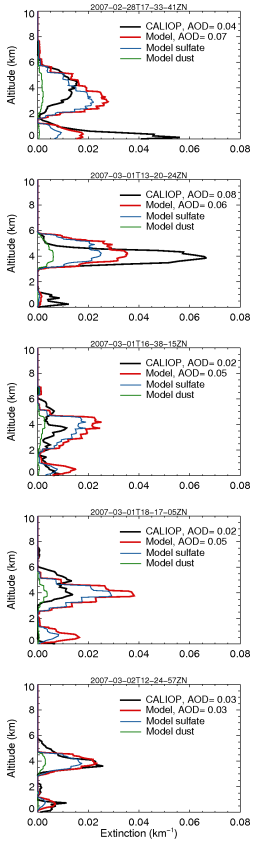

Fig. 4. CALIOP (black) and GEOS-Chem (red) mean aerosol extinction profiles for the regions highlighted by red boxes in Fig. 2. The CALIOP sensitivity threshold is applied to the modeled extinction profiles. The green and blue lines represent the extinction attributed to dust and sulfate respectively. The modeled and observed AOD, calculated by integration of the extinction profile over the vertical extent of each plume are listed on each panel.

ACPD
10, 25389–25433, 2010

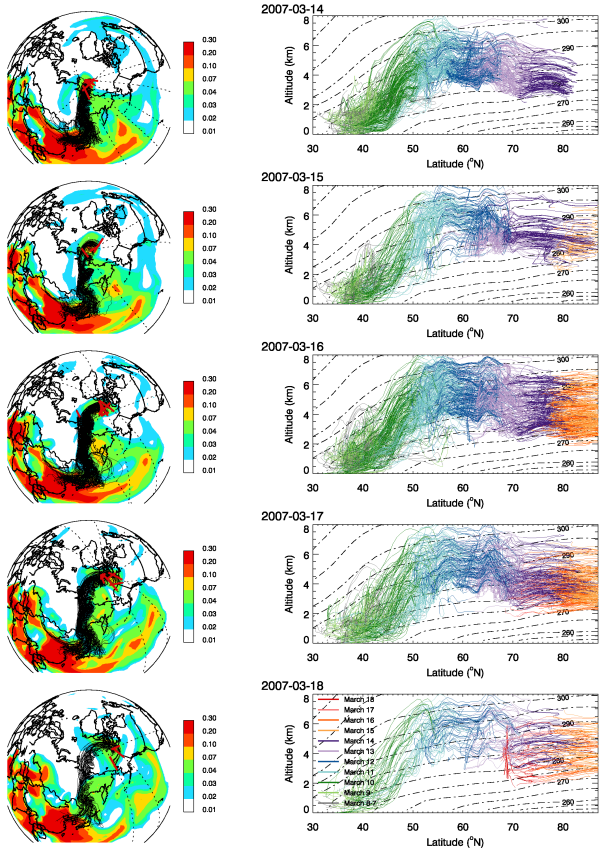

Fig. 5. Same as Fig. 1 but for 14–18 March, 2007. The potential temperature contours (right panels) are zonally and temporally averaged in the longitude interval [110° E, 160° W] from 9 March, 0Z until the time when the last plume was observed, for each day.

ACPD
10, 25389–25433, 2010

Satellite observations of aerosol transport from East Asia to the Arctic

M. Di Pierro et al.

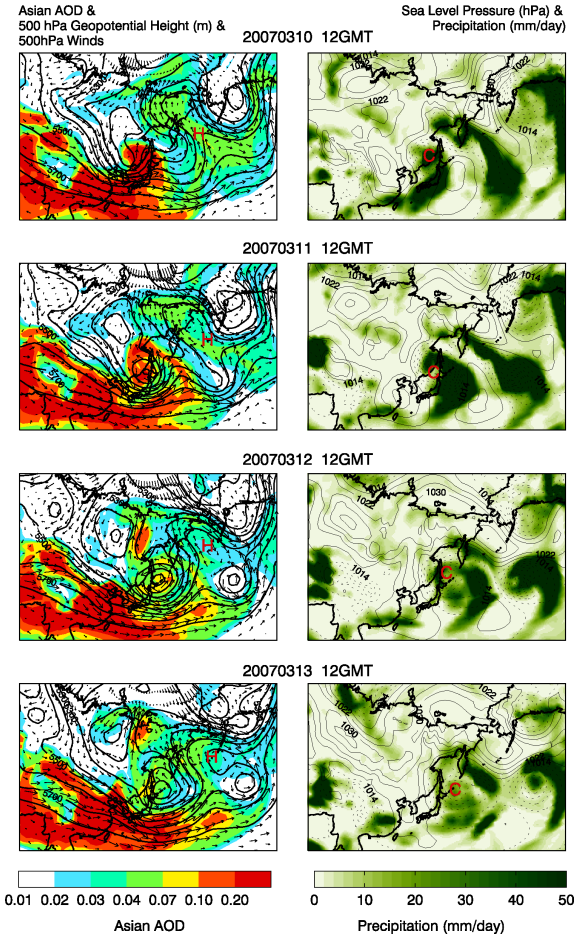

Fig. 6. Synoptic situation during the initial stages of the export event of 12–19 March 2007. Conventions are the same as in Fig. 3.

ACPD
10, 25389–25433, 2010

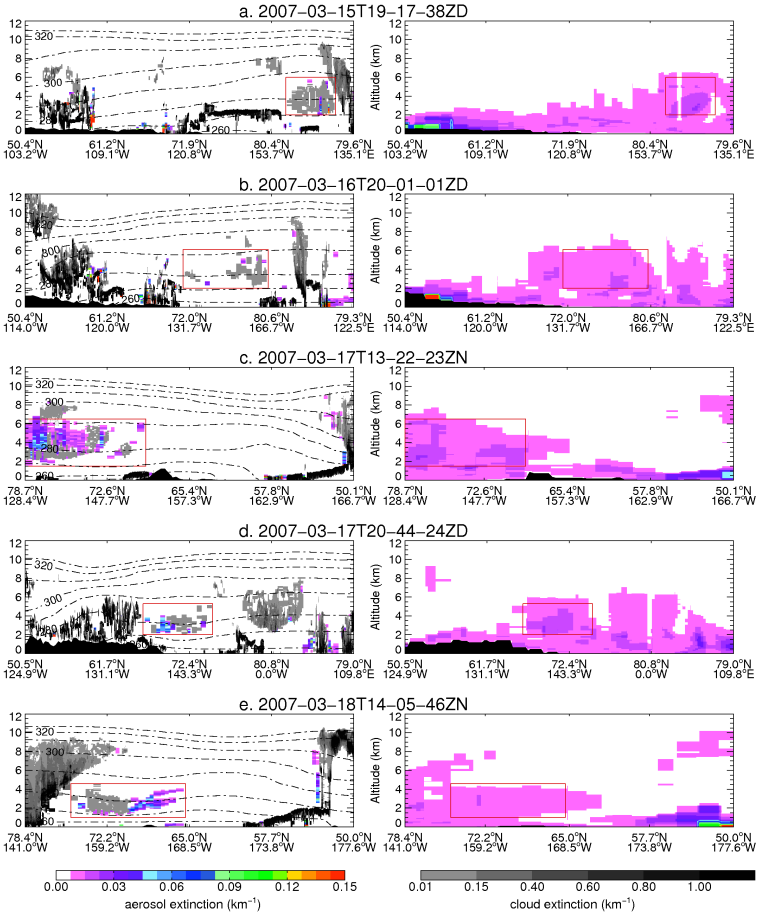

Fig. 7. Same as Fig. 2a for a subset of five major plume cross sections for the 12–19 March event. The red box delimits the aerosol plume cross sections, which are sometimes misclassified as clouds (see text).

ACPD
10, 25389–25433, 2010

Satellite observations of aerosol transport from East Asia to the Arctic

M. Di Pierro et al.

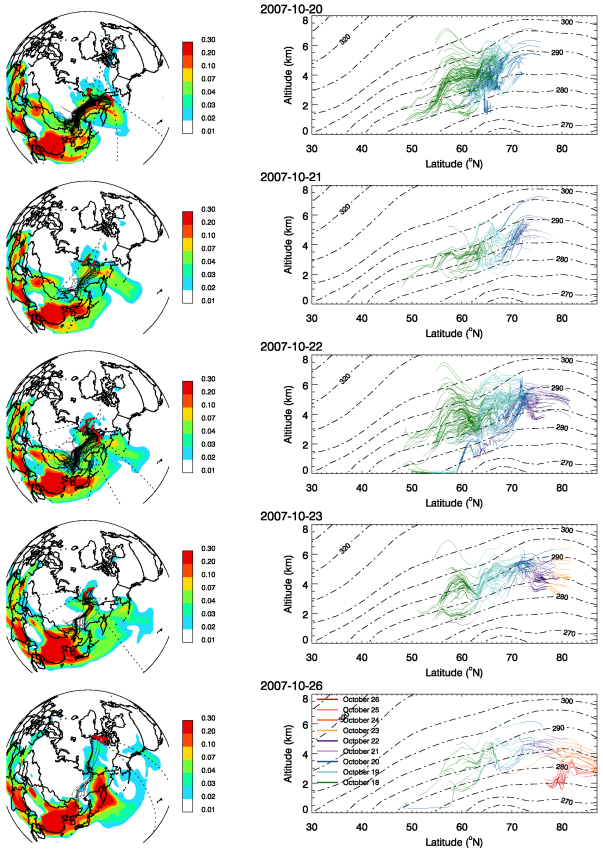

Fig. 8. Same as Fig. 1, but for the 20–27 October, 2007 event. The potential temperature contours are zonally and temporally averaged in the longitude interval [100° E, 180° E] from 17 October, 0Z until the time when the last plume was observed, for each day.

ACPD
10, 25389–25433, 2010

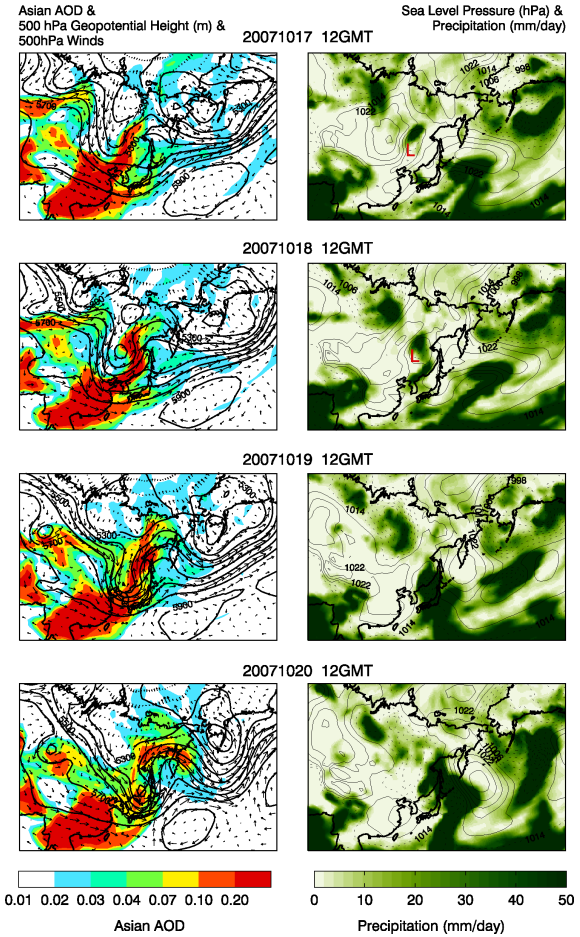

Fig. 9. Synoptic situation during the initial stages of the export event of 20–27 October. Conventions are the same as in Fig. 3.

ACPD
10, 25389–25433, 2010

Satellite observations of aerosol transport from East Asia to the Arctic

M. Di Pierro et al.

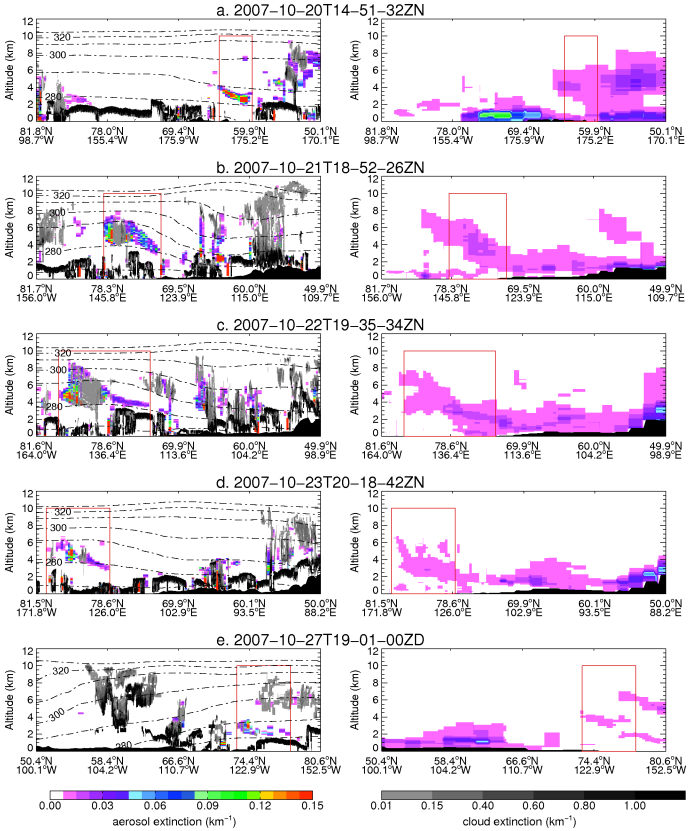

Fig. 10. Same as Fig. 2a, for a subset of five major plume cross sections for the 20–27 October event.

ACPD
10, 25389–25433, 2010

Satellite observations of aerosol transport from East Asia to the Arctic

M. Di Pierro et al.

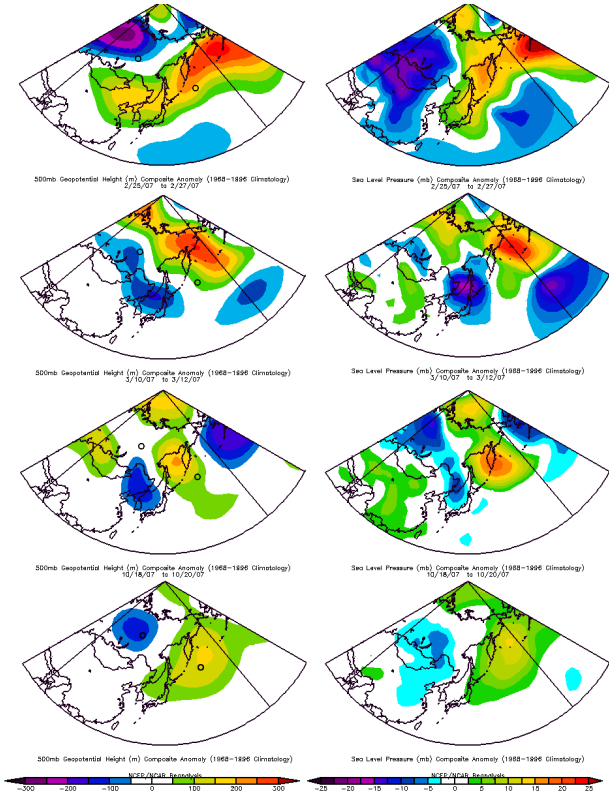

Fig. 11. 500 hPa Geopotential height anomaly pattern (left panels) and Sea Level Pressure anomaly (right panels) for the 3-day initial stage of export to the Arctic of the three case studies discussed here: 25–27 February, 10–12 March, and 18–20 October. Bottom panels: composite of all eleven episodes observed by CALIOP in 2007–2009. Two circles indicate the location of the two poles used to define the AME index. Images provided by the NOAA/ESRL Physical Sciences Division, Boulder Colorado from their Web site at http://www.esrl.noaa.gov/psd/.

ACPD
10, 25389–25433, 2010

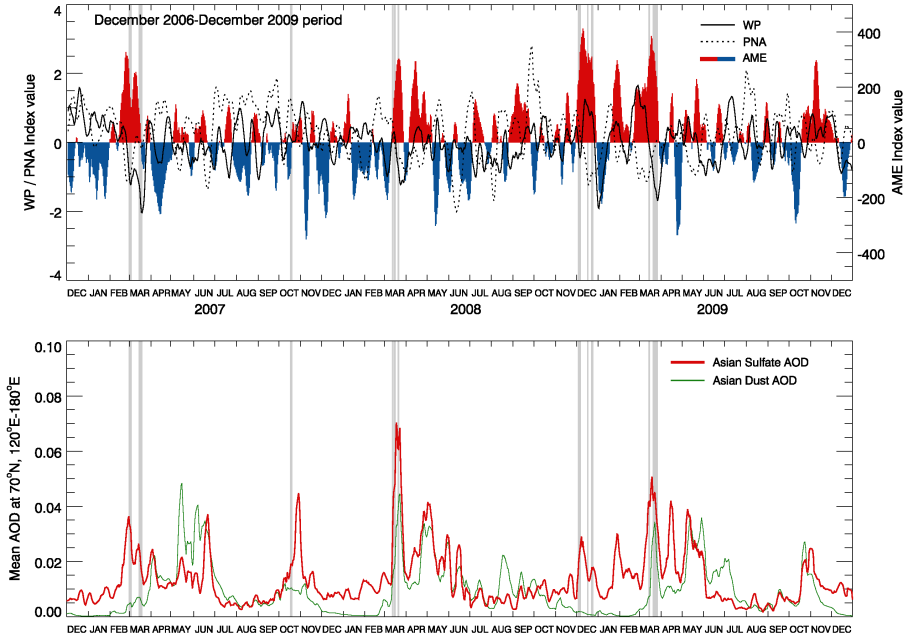

Fig. 12. Timeseries of meteorological indices and Asian AOD for December 2006–December 2009. Top panel: WP, PNA, and AME (red=positive, blue=negative) timeseries. A two-day lag is applied to all indices. Bottom panel: Asian Sulfate and Asian Dust AOD calculated by GEOS-Chem at 70° N averaged between 120° E and 180° E. All timeseries are smoothed with a 7-day running mean. The vertical grey bars show the 11 instances when CALIOP intercepted Asian plumes over the Arctic.

ACPD
10, 25389–25433, 2010